Mon. Not. R. Astron. Soc. **000**, 000–000 (0000) Printed 22 December 2001 (MN LaTeX style file v1.4)

Impact of reverberation in flared accretion discs on temporal characteristics of X-ray binaries

Juri Poutanen*
Astronomy Division, P.O. Box 3000, 90014 University of Oulu, Finland
Stockholm Observatory, 10691 Stockholm, Sweden

Accepted, Received

ABSTRACT
Observations suggest that accretion discs in many X-ray binaries are likely flared. An outer edge of the disc intercepts radiation from the central X-ray source. Part of that radiation is absorbed and reemitted in the optical/UV spectral ranges. However, a large fraction of that radiation is reflected and appears in the broad-band X-ray spectrum as a Compton reflection bump. This radiation is delayed and variability is somewhat smeared compared with the intrinsic X-ray radiation. We compute response functions for flat and flared accretion discs and for isotropic and anisotropic X-ray sources. A simple approximation for the response function which is valid in the broad range of the disc shapes and inclinations, inner and outer radii, and the plasma bulk velocity is proposed. We also study the impact of the X-ray reprocessing on temporal characteristics of X-ray binaries such as the power spectral density, auto- and cross-correlation functions, and time/phase lags. We propose a reprocessing model which explains the secondary peaks in the phase lag Fourier spectra observed in Cyg X-1 and other Galactic black hole sources. The position of the peaks could be used to determine the size of the accretion disc.

Key words: accretion, accretion discs – black hole physics – methods: numerical – stars: individual: Cygnus X-1 – X-rays: binaries

1 INTRODUCTION

The X-ray spectra of radio-quiet active galactic nuclei (AGNs) and X-ray binaries can often be decomposed into a power-law like continuum with a cutoff at 100 keV (Zdziarski 1999), soft black body emission from the accretion disc and/or neutron star surface, and the Compton reflection continuum with the associated iron emission line at $\sim$ 6.4 keV (see e.g. George & Fabian 1991; Nandra & Pounds 1994; Reynolds 1999). The reflection features are produced in a rather cold neutral material which is often identified with an accretion disc. Correlation between the amplitude of reflection, R, and the photon spectral index, Γ, in X-ray binaries and AGNs (Zdziarski, Lubiński & Smith 1999; Gilfanov, Churazov & Revnivtsev 2000a) implies that a relatively large fraction of reflection originates close to the X-ray emitting region. In the case of X-ray binaries, some fraction of reflected photons, however, can also come from a companion star (Basko, Titarchuk & Sunyaev 1974; Done & Życki 1999; Vikhlinin 1999) or an outer part of the accretion disc. In the case of AGNs, the delayed reflection from a distant molecular torus (e.g. Ghisellini, Haardt & Matt 1994) can be clearly observed when the central X-ray source turns off (Guainazzi et al. 1998).

The reflected radiation is necessarily delayed relative to the direct radiation from the X-ray source. Studies of these delays can help to determine the geometry of the accretion disc, the position of the X-ray source, and the distance to the companion (Vikhlinin 1999). A number of papers were devoted to studies of the response of the Fe line profile to an X-ray flare in the vicinity of a black hole (e.g. Reynolds et al. 1999; Hartnoll & Blackman 2000). Observations of AGNs with future X-ray missions such as Constellation-X may open a possibility of determining directly from the Fe line profile temporal evolution, the geometry of the X-ray emitting region and the mass and spin of black holes (see Reynolds 1999; Fabian et al. 2000 for reviews). However, in order to do that, observation of a bright individual flare is needed. Otherwise, the interpretation of the line profile produced by many flares would be complicated. Such studies are impossible in the case of X-ray binaries even with future instruments since the photon flux per light crossing time of one gravitational radius is thousands times smaller than in AGNs. As an alternative to studying the line profiles one can use the whole available statistics at different energy bands and analyse the response of the reflected *continuum* radiation to a varying X-ray source.

All the temporal studies mentioned above assumed that the accretion disc is flat. In contrast, a number of observations indicate that accretion discs are flared, i.e. geometrically thick at the outer edge (see Verbunt 1999 for a recent review). There observations include obscurations of the central X-ray source (e.g. White &

* E-mail: juri.poutanen@oulu.fi

Holt 1982) and the variability properties in the UV/optical/infrared spectral band in low-mass X-ray binaries (e.g. Mason & Cordova 1982; Vrtilek et al. 1990), the delays between the optical/UV emission and the X-rays observed in the X-ray bursters (Trümper et al. 1985) and in the super-luminal black hole source GRO J1655-40 (Hynes et al. 1998). The inferred height-to-radius ratio, $H/r_{\rm out}$, at the outer edge of the disc varies from 0.15 to 0.5. This is much larger than predicted by the standard accretion disc theory (Shakura & Sunyaev 1973).

In this paper, we study the impact of the X-ray reflection from flat and flared accretion discs on temporal characteristics of the X-ray binaries and AGNs. In § 2, we present the general formalism for computation of the response functions and introduce approximations that allow one to consider a linear reflection response. Formulae describing the impact of reflection on the temporal characteristics of the composite (direct and reflected) signal are presented in § 3. Response functions for the flat and flared discs and the resulting phase lags are presented in § 4. Comparison with observations and discussion is given in § 5. Conclusions are presented in § 6.

2 RESPONSE FROM THE ACCRETION DISC

2.1 General formulation

Let us consider an axially-symmetric accretion disc and assume for simplicity that the height of the disc surface above the equatorial plane is given by a power-law relation

$$z(r) = H(r/r_{\rm out})^{\alpha}, \qquad (1)$$

where H is the maximum disc height, $r_{\rm out}$ is the disc radius, and $\alpha \geq 1$. The inner radius of the disc is $r_{\rm in}$. Throughout this paper, distances will be measured in units of $R_{\rm g} \equiv 2GM/c^2$ and time– in units of $R_{\rm g}/c$. For all the examples considered below, we take $M = 10{\rm M}_{\odot}$, but the results can be easily scaled to any mass.

Let us introduce the Cartesian coordinate system with the origin at the disc center. The x- and y-axes lie in the central disc plane, and the line of sight towards the observer is in the $x-z$ plane in the direction $\boldsymbol{o} = (\sin i, 0, \cos i)$, where i is the inclination. The geometry of the problem is presented in Fig. 1. An X-ray point source is situated at the disc axis at some height h from the disc plane, i.e. at the position $\boldsymbol{h} = (0, 0, h)$. Let us assume that the X-ray source angular distribution does not depend on time and photon energy. The direct (marked with a superscript D) monochromatic luminosity (per unit solid angle) is then

$$L_E^{\rm D}(\mu, t) = L_E^{\rm D}(t)\frac{\Omega(\mu)}{4\pi}. \qquad (2)$$

The total emitted luminosity is then

$$L^{\rm D}(t) = \int {\rm d}E \int_{-1}^{1} {\rm d}\mu 2\pi L_E^{\rm D}(\mu, t). \qquad (3)$$

Function $\Omega(\mu)$ gives the dependence of the incident (direct) radiation field on zenith angle $\arccos\mu$, and is normalised $\frac{1}{2}\int \Omega(\mu){\rm d}\mu = 1$, i.e. for an isotropic source, $\Omega(\mu) = 1$.

An element of the disc surface has coordinates $\boldsymbol{d} = (r\cos\phi, r\sin\phi, z)$, where the azimuth ϕ is measured from the x-axis. Photons reflected from that element are delayed by

$$\Delta t(r, \phi) = p - \boldsymbol{p}\cdot\boldsymbol{o} = p - r\sin i\cos\phi - (z-h)\cos i \qquad (4)$$

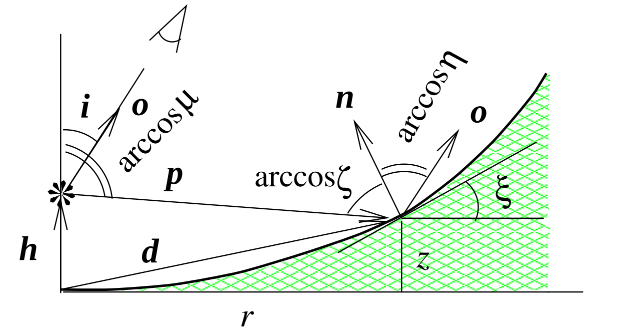

Figure 1. Geometry of the problem. Note that vector $\boldsymbol{o}$ does not generally lie in the plane defined by other vectors.

relative to the photons reaching the observer directly. Here $\boldsymbol{p} = \boldsymbol{d} - \boldsymbol{h}$ and $p = \sqrt{r^2 + (z-h)^2}$ is the distance between the source and the reflection point.

The temporal evolution of the radiation reflected towards the observer can be described by the following relation:

$$L_E^{\rm refl}(\cos i, t) = \int_{r_{\rm m}}^{r_{\rm M}} r{\rm d}r \int_0^{2\pi} F_E(\eta, \zeta, r, \phi, t){\rm d}\phi, \qquad (5)$$

where $r_{\rm m}, r_{\rm M}$ are the innermost and outermost disc radii intersecting the isodelay paraboloid (see § 2.5 and Appendix A3) and

$$F_E(\eta, \zeta, r, \phi, t) = \frac{\Omega(\mu)}{4\pi p^2}\frac{\zeta}{\cos\xi}\frac{2\eta}{2\pi} \times \int_E^{\infty} \mathcal{R}(r; E, \eta; E', \zeta) L_{E'}^{\rm D}(t - \Delta t){\rm d}E' \qquad (6)$$

is the monochromatic flux of radiation reflected in a unit solid angle from a surface element that gives a unit area when projected onto the central plane (note factor $\cos\xi = 1/\sqrt{1+z'^2}$ in the denominator, where $z' = \partial z/\partial r$). The reflection Green function $\mathcal{R}$ describes the processes of Compton reflection, photoelectric absorption, and fluorescent line emission (see e.g. Poutanen, Nagendra & Svensson 1996). It depends on the angles $\arccos\zeta$, $\arccos\eta$ between the normal $\boldsymbol{n}$ to the disc surface at a reflection point and the directions of the incoming and outgoing photons, respectively, as well as on the photon energies. Here

$$\begin{aligned}\zeta &= -\boldsymbol{n}\cdot\boldsymbol{p}/p = [r\sin\xi - (z-h)\cos\xi]/p,\\ \eta &= \boldsymbol{n}\cdot\boldsymbol{o} = -\sin i\sin\xi\cos\phi + \cos\xi\cos i,\\ \mu &= (z-h)/p.\end{aligned} \qquad (7)$$

In principle, there exists a weak dependence of $\mathcal{R}$ on the difference in the azimuth of incoming and outgoing photons, which we neglect. This is equivalent to assuming isotropic scattering. The reflection Green function can also be a function of radius, for example, if the ionisation state of the disc changes with radius.

It is worth noticing that the evolution of the reflected radiation (eq. 5) depends not only on time, photon energy, and inclination angle, but also on the shape of the intrinsic spectrum $L_E^{\rm D}(t)$. Thus, in general, temporal characteristics of the reflected radiation at a given photon energy E depend on behaviour of the intrinsic spectrum at *all* energies above E. This means that there is *no* linear response between the intrinsic and reflected signals at a single energy E. In a number of physically realistic situations considered below the response is, however, very close to linear. That helps us to solve temporal problems in a simpler way.

2.2 Constant intrinsic spectrum

If the spectrum of the intrinsic X-ray radiation $L_E^{\rm D}(t)$ does not vary in time while the normalisation varies,

$$L_E^{\rm D}(t) = P(t) L^{\rm D}(E), \tag{8}$$

equation (6) can be simplified:

$$F_E(\eta,\zeta,r,\phi,t) = L_E^{\rm D}(t-\Delta t)\frac{\Omega(\mu)}{4\pi p^2}\frac{\zeta}{\cos\xi}\frac{2\eta}{2\pi}\rho_E(r,\eta,\zeta), \tag{9}$$

where we introduced the angle- and energy-dependent albedo function

$$\rho_E(r,\eta,\zeta) = \int_E^\infty \mathcal{R}(r;E,\eta;E',\zeta)L^{\rm D}(E'){\rm d}E'/L^{\rm D}(E). \tag{10}$$

The temporal and all other variables are separated. The temporal evolution of the reflected radiation at energy E and inclination i can be represented as a convolution of the direct luminosity at the same angle i with the energy- and inclination-dependent response (transfer) function:

$$L_E^{\rm refl}(\cos i, t) = \int_{-\infty}^{t} T_E(t-t')L_E^{\rm D}(\cos i, t'){\rm d}t', \tag{11}$$

$$\begin{aligned} T_E(t) &= \int r{\rm d}r \int_0^{2\pi} \delta(t-\Delta t){\rm d}\phi \\ &\times \frac{\zeta}{p^2\cos\xi}\frac{\Omega(\mu)}{\Omega(\cos i)}\frac{2\eta}{2\pi}\rho_E(r,\eta,\zeta). \end{aligned} \tag{12}$$

The total observed luminosity is thus presented as a sum of the direct and reflected luminosities:

$$L_E(\cos i,t) = L_E^{\rm D}(\cos i,t) + \int_{-\infty}^{t} T_E(t-t')L_E^{\rm D}(\cos i,t'){\rm d}t'. \tag{13}$$

2.3 Thomson approximation

X-ray observations with high temporal resolution and large photon statistics exist only at moderate energies ($E \lesssim 20$ keV), for which in the first approximation Compton recoil can be neglected, and the reflection Green function then takes the form

$$\mathcal{R}(r;E,\zeta;E',\eta) = \rho_E(r,\eta,\zeta)\delta(E-E'). \tag{14}$$

In the Thomson approximation (14), the energy integral in equation (6) can be trivially taken. It is easy to see that the reflected radiation is then given by equation (11) with the response function (12).

A specific form of the function ρ_E depends on the properties of the reflecting medium. If, for example, the medium is homogeneous, i.e. the single-scattering albedo (the ratio of Thomson cross-section to the sum of Thomson and photoelectric cross-sections), $\lambda = \sigma_{\rm T}/(\sigma_{\rm ph}+\sigma_{\rm T})$, is constant with depth, the reflection Green function ρ_E can be presented as a product of two Ambarzumian functions (see e.g. Chandrasekhar 1960; Sobolev 1975)

$$\rho_E(\eta,\zeta) = \frac{\lambda}{4}\frac{H_\lambda(\eta)H_\lambda(\zeta)}{\eta+\zeta}, \tag{15}$$

and is normalised to the reflection albedo:

$$\int_0^1 \rho_E(\eta,\zeta)2\eta{\rm d}\eta = a_E(\zeta) = 1 - H_\lambda(\zeta)\sqrt{1-\lambda}. \tag{16}$$

For an isotropic source above the infinite plane the angle-averaged albedo then

$$a_E = \int_0^1 a_E(\zeta){\rm d}\zeta = 1 - h_0\sqrt{1-\lambda}, \tag{17}$$

where $h_0 = 2(1-\sqrt{1-\lambda})/\lambda$ is the zeroth moment of H_λ. The function H_λ satisfies the integral equation

$$H_\lambda(\eta) = 1 + \frac{\lambda}{2}\eta H_\lambda(\eta)\int_0^1 \frac{H_\lambda(\zeta){\rm d}\zeta}{\eta+\zeta}. \tag{18}$$

For $\lambda \ll 1$,

$$H_\lambda(\eta) \approx 1 + \frac{\lambda}{2}\eta\ln\frac{1+\eta}{\eta}, \quad a_E \approx \frac{\lambda}{4}. \tag{19}$$

One should note that the response function depends on the photon energy through the function ρ_E.

2.4 Isotropic approximation

The response function in general depends on the properties of the Green function for reflection which is a function of the photon energy and possibly radius (see eq. 12). However, if the physical conditions do not change with radius and if one assumes that the intensity of the reflected radiation is isotropic (we will call this the isotropic approximation), one can approximate $\rho_E(r,\eta,\zeta) = a_E$. In this case, one can introduce a response function that is independent of albedo and photon energy:

$$T(t) \equiv \frac{T_E(t)}{a_E} = \int r{\rm d}r\int_0^{2\pi}\delta(t-\Delta t){\rm d}\phi\frac{\zeta}{p^2\cos\xi}\frac{\Omega(\mu)}{\Omega(\cos i)}\frac{2\eta}{2\pi}. \tag{20}$$

The advantage of this approximation is that we need to compute only one response function. In most applications considered in this paper we use this approximation. We discuss its accuracy in § 4.4.1.

2.5 Integration over azimuth and radius

In order to integrate expressions (12) and (20) over the azimuth one can use the following identity:

$$\begin{aligned} G(r,t) &\equiv \int_0^{2\pi}\delta(t-\Delta t){\rm d}\phi \\ &= \frac{2}{r\sin i\,|\sin\phi|} \\ &= \begin{cases} 2/\sqrt{r^2\sin^2 i - [t-p+(z-h)\cos i]^2}, & i\neq 0, \\ 2\pi\delta(t-p+z-h), & i = 0. \end{cases} \end{aligned} \tag{21}$$

For given t and r, the azimuth ϕ is found from equation (4) (note that p and z are functions of r only)

$$\cos\phi = -\frac{t-p+(z-h)\cos i}{r\sin i}. \tag{22}$$

The limits $r_{\rm m}, r_{\rm M}$ in equation (5) are determined by the conditions that expression under square root in (21) is positive (i.e. $|\cos\phi| <$

1, eq. 22) and that $r_{\rm in} \le r_{\rm m} < r_{\rm M} \le r_{\rm out}$. The details on the method of integration over the radius in equation (5) are given in the Appendix.

3 TEMPORAL CHARACTERISTICS

As we showed in § 2.2 and § 2.3, the reflected signal depends linearly on the intrinsic (direct) signal when there is no spectral variability of the direct radiation or at sufficiently low energies where Compton down-scattering can be ignored. Timing properties of the reflected radiation are then described by a response function $T_E(t)$. For most of our applications, we assume that albedo does not depend on radius and one can take $T_E(t) = a_E T(t)$, where now $T(t)$ is energy independent. The total observed radiation flux is composed of the direct radiation from the X-ray source plus the radiation reflected from the disc (see eq. 13):

$$L_E(t) = L_E^{\rm D}(t) + a_E \int_{-\infty}^{t} T(t-t') L_E^{\rm D}(t') {\rm d}t'. \tag{23}$$

The cross-correlation function (CCF) of the total signal, $C_{12}(t) = \int L_1(t') L_2(t'+t){\rm d}t'$, can be easily found substituting equation (23):

$$\begin{aligned} C_{12}(t) &= C_{12}^{\rm D}(t) + a_1 a_2 \int_{-\infty}^{\infty} C_{12}^{\rm D}(t') A^{\rm T}(t-t'){\rm d}t' \\ &+ \int_{-\infty}^{\infty} C_{12}^{\rm D}(t') \left[a_2 T(t-t') + a_1 T(t'-t)\right] {\rm d}t', \end{aligned} \tag{24}$$

where $C_{12}^{\rm D}(t)$ is the CCF of the direct signal and $A^{\rm T}(t) = \int T(t')T(t'+t){\rm d}t'$ is the auto-correlation of the response function. The auto-correlation function (ACF) can be obtained from the above expression:

$$\begin{aligned} A_E(t) &= A_E^{\rm D}(t) + a_E^2 \int_{-\infty}^{\infty} A_E^{\rm D}(t') A^{\rm T}(t-t'){\rm d}t' \\ &+ a_E \int_{-\infty}^{\infty} A_E^{\rm D}(t')[T(t'+t) + T(t'-t)]{\rm d}t', \end{aligned} \tag{25}$$

where $A_E^{\rm D}(t)$ is the ACF of the direct signal.

The Fourier transform of (23) reads

$$\hat{L}_E(f) = \hat{L}_E^{\rm D}(f)[1 + a_E \hat{T}(f)]. \tag{26}$$

The cross-spectrum of the light curves at two energies E_1, E_2, $\hat{C}_{12}(f) \equiv [\hat{L}_1(f)]^* \hat{L}_2(f)$, can be expressed as a product

$$\hat{C}_{12}(f) = \hat{C}_{12}^{\rm D}(f) \hat{C}_{12}^{\rm R}(f) = |\hat{C}_{12}^{\rm D}(f)| e^{i\varphi_{\rm D}(f)} |\hat{C}_{12}^{\rm R}(f)| e^{i\varphi_{\rm R}(f)}, \tag{27}$$

where $\hat{C}_{12}^{\rm D}(f) = [\hat{L}_1^{\rm D}(f)]^* \hat{L}_2^{\rm D}(f)$ is the cross-spectrum of the direct radiation and

$$\hat{C}_{12}^{\rm R}(f) \equiv 1 + a_1 a_2 |\hat{T}(f)|^2 + a_1 \hat{T}^*(f) + a_2 \hat{T}(f). \tag{28}$$

The phase lags of the direct radiation $\varphi_{\rm D}(f)$ and that added by reflection $\varphi_{\rm R}(f)$ are defined as the phases of $\hat{C}_{12}^{\rm D}(f)$ and $\hat{C}_{12}^{\rm R}(f)$, respectively. The "reflection" phase lag,

$$\tan\varphi_{\rm R}(f) = \frac{(a_2 - a_1)\Im\hat{T}(f)}{1 + (a_1 + a_2)\Re\hat{T}(f) + a_1 a_2 |\hat{T}(f)|^2}, \tag{29}$$

is positive (hard lags) when $a_2 > a_1$. Here $\Re$ and $\Im$ denote real and imaginary part of a complex variable. For small a_1 and small $a_2 \int T(t){\rm d}t$, the phase lag is approximately:

$$\varphi_{\rm R}(f) \approx (a_2 - a_1)\Im\hat{T}(f). \tag{30}$$

The power density spectra (PDS) are related in the following way:

$$|\hat{L}_E(f)|^2 = |\hat{L}_E^{\rm D}(f)|^2 \left[1 + a_E^2 |\hat{T}(f)|^2 + 2a_E \Re\hat{T}(f)\right]. \tag{31}$$

In many recent publications, the PDS is often normalised to the relative rms of the signal (Miyamoto et al. 1991; Nowak et al. 1999a). We denote such a PDS $P(f)$. In this normalisation, we get

$$P(f) = P^{\rm D}(f) \frac{1 + a_E^2 |\hat{T}(f)|^2 + 2a_E \Re\hat{T}(f)}{\left[1 + a_E \int T(t){\rm d}t\right]^2}. \tag{32}$$

4 RESULTS

4.1 Simple response functions

For illustration, let us specify a simple exponential response function:

$$T(t) = \begin{cases} R\exp[-(t-\tau)/\tau]/\tau, & t \ge \tau, \\ 0, & t < \tau. \end{cases} \tag{33}$$

The corresponding Fourier transform is $\hat{T}(f) = R\exp(ix)/(1 - ix)$, where $x = 2\pi f \tau$. As a starting point let us take $E_1 = 3$ keV where for the neutral reflector of solar abundances the albedo $a_1 \sim 0.014$. This is the smallest energy available for timing analysis, for example, at *RXTE*. For $a_E \gg a_1$, the phase lag at energy E relative to E_1 is then

$$\tan\varphi_E^{\rm R}(f) \approx \frac{a_{\rm eff}(x\cos x + \sin x)}{1 + x^2 + a_{\rm eff}(\cos x - x\sin x)}, \tag{34}$$

where $a_{\rm eff} = R a_E$ is the effective albedo. The phase lag grows linearly with frequency as $\varphi_E^{\rm R}(f) \approx 2a_{\rm eff} x/(1 + a_{\rm eff})$ for $x \ll 1$, and for $a_{\rm eff} \lesssim 3$ reaches the maximum $\tan\varphi_{\rm max,1}^{\rm R} \approx 0.7a_{\rm eff}/(1 - 0.15a_{\rm eff})$ at $x \approx 1$ (see Fig. 2a). The peak shift slightly towards higher frequencies at larger $a_{\rm eff}$. When $a_{\rm eff} \gtrsim 3$ (large effective albedo is possible in strongly anisotropic sources), phase lag goes through π at $x \sim 2$. For $a_1 \ll a_{\rm eff} \ll 1$ and $x \ll 1$, the phase lags are proportional to the albedo a_E (see eq. 30), and their energy dependence is exactly the same as that a_E. At small energies close to E_1, lags go to zero. At larger energies (and larger albedos), the phase lag rises slower than a_E (Fig. 2b). At large frequencies, when $\cos x \sim x\sin x$ (i.e. $x \sim 1$), the dependence on a_E in the denominator of eq. (34) disappears and $\varphi_E^{\rm R}$ depends linearly on a_E. Including the fluorescent iron line would produce a bump in the phase lag energy spectrum which amplitude depends on the energy resolution of the X-ray instrument.

If the response function is a sum of two exponentials described by τ_1, R_1 and τ_2, R_2, respectively (let $\tau_1 \ll \tau_2$), the phase lag has two prominent maxima at $f_1 \sim 1/(2\pi\tau_1)$ and $f_2 \sim 1/(2\pi\tau_2)$. The value of the high frequency maximum at f_1 is the same as for the case of a single reflector, while the new, low frequency maximum is $\tan\varphi_{\rm max,2}^{\rm R} \approx 0.7a_{\rm eff,2}/[1 + a_{\rm eff,1} - 0.15a_{\rm eff,2}]$.

Let us now consider the effect of reflection on the shape of the auto- and cross-correlation functions. The effect is easier to understand if one considers an even simpler δ-function response $T(t) = R\delta(t-\tau)$. Then

$$A_E(t) = (1 + a_E^2 R^2) A_E^{\rm D}(t) + a_E R[A_E^{\rm D}(t-\tau) + A_E^{\rm D}(t+\tau)]. \tag{35}$$

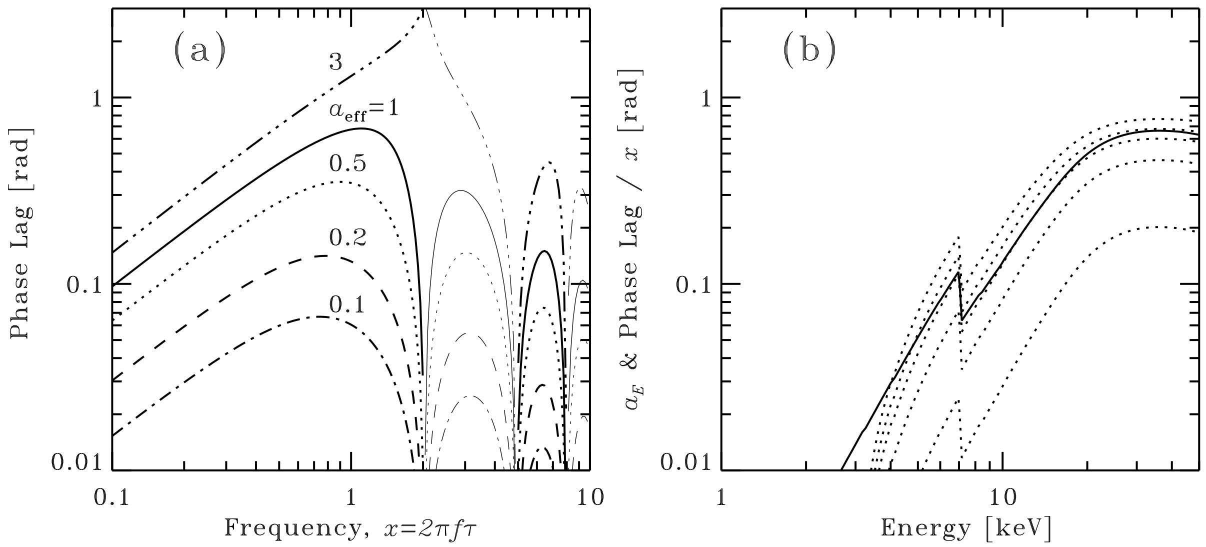

Figure 2. Phase lags for the exponential response function (33). (a) $\varphi_E^{\rm R}(f)$ frequency dependence for different $a_{\rm eff}$ relative to 3 keV (where $a_1 = 0.014$). Thin curves give the negative phase lags. (b) Solid curve gives the angle-averaged albedo a_E for Compton reflection from neutral medium (omitting Fe Kα line) corresponding to the intrinsic photon power-law index $\Gamma = 2$ computed for solar abundances using pexrav model (Magdziarz & Zdziarski 1995) from XSPEC. Dotted curves give the energy dependence of the phase lag $\varphi_E^{\rm R}(f)$ (relative to 3 keV) divided by frequency $x \equiv 2\pi f\tau$ for $R = 1$ at frequencies $x = 0.1, 0.5, 0.7, 1, 1.5$ (from top to bottom). At $x < 0.1$, the curves coincide with the $x = 0.1$ case.

For monotonic, strongly peaked at zero lag ACF (such as that of Cyg X-1, see Maccarone, Coppi & Poutanen 2000) and $a_E \ll 1$, the largest relative increase in the total ACF achieved at lag $\sim \tau$ is $\sim 1 + a_E R / A_E^{\rm D}(\tau)$ (for the normalised to unity at zero lag ACF). This means that the changes are more significant when the characteristic decay time-scale of the ACF is smaller than or comparable to the characteristic delay due to reflection. Similar behaviour is expected for the exponential response function (33).

The CCF for $a_1 = 0$ and δ-function response takes the form:

$$C_{12}(t) = C_{12}^{\rm D}(t) + a_2 R C_{12}^{\rm D}(t - \tau). \tag{36}$$

Since the CCFs of most GBHs and AGNs are strongly peaked at zero lag (see e.g. Nolan et al. 1981; Papadakis & Lawrence 1995; Smith & Liang 1999; Lee et al. 2000; Maccarone et al. 2000), the total observed CCF should become more asymmetric for larger albedos (i.e. at larger energies). The largest relative deviation from the intrinsic CCF should be observed at lags $t \sim \tau$. In the case of the intrinsic CCF $C_{12}^{\rm D}(t) = \exp[-(t/t_0)^\nu]$, the relative change at large lags, $|t| \gg \tau$, is the following:

$$\frac{C_{12}(t)}{C_{12}^{\rm D}(t)} = 1 + a_2 R \exp\left[{\rm sgn}(t) \nu \frac{\tau |t|^{\nu-1}}{t_0^\nu} \right]. \tag{37}$$

4.2 Flat disc response

4.2.1 Infinite slab

The response function for a flat disc and an isotropic source can be derived analytically from equation (20) in the isotropic approximation (i.e. $\rho = a_E$). In this case, $z = 0$, $\cos\xi = 1$, $\eta = \cos i$, $\zeta = h/p$, and

$$T_{\rm slab}(t) = \frac{2\cos i}{2\pi} \int \frac{r\,{\rm d}r}{p^2} \frac{h}{p} G(r,t), \tag{38}$$

where $p^2 = r^2 + h^2$ and $G(r,t)$ is given by equation (21). The variable p should satisfy the condition $p_- < p < p_+$, where

$$p_\pm = q \pm s,\ q = \frac{t - h\cos i}{\cos^2 i},\ s = \frac{\sin i \sqrt{t(t - 2h\cos i)}}{\cos^2 i}. \tag{39}$$

Substituting $p = q + s\cos\theta$ into equation (38) we get:

$$\begin{aligned} T_{\rm slab}(t) &= \frac{2\cos i}{2\pi} \int\limits_{p_-}^{p_+} \frac{h{\rm d}p}{p^2} \frac{2}{\cos i \sqrt{(p - p_-)(p_+ - p)}} \\ &= \frac{2h}{\pi} \int\limits_0^\pi \frac{{\rm d}\theta}{(q + s\cos\theta)^2} = \frac{2h}{\pi} \frac{\pi q}{(q^2 - s^2)^{3/2}} \\ &= 2\cos i \frac{h(t - h\cos i)}{(t^2 + h^2 - 2th\cos i)^{3/2}}, \quad t \geq 2h\cos i. \end{aligned} \tag{40}$$

The response function is normalised in the following way:

$$\int\limits_{2h\cos i}^{\infty} T_{\rm slab}(t){\rm d}t = 2\cos i. \tag{41}$$

4.2.2 Disc with a central hole

In hot flow models for the X-ray production in accreting black holes, the X-ray source is situated inside a cold accretion disc truncated at some radius (see e.g. Esin et al. 1998; Poutanen 1998). The response then can be approximately evaluated assuming a point source at the axis of the disc with $r_{\rm in} \gg 1$ (see also Gilfanov, Churazov & Revnivtsev 2000b). A more general expression for the response function, for a non-zero inner radius and a finite outer radius $r_{\rm out}$, can be written similarly to equation (40):

$$\begin{aligned} T(t) &= \frac{2h}{\pi} \int\limits_{p_{\rm m}}^{p_{\rm M}} \frac{{\rm d}p}{p^2 \sqrt{(p - p_-)(p_+ - p)}} \\ &= \frac{2h}{\pi} \int\limits_{\theta_{\rm M}}^{\theta_{\rm m}} \frac{{\rm d}\theta}{(q + s\cos\theta)^2}, \quad t_{\rm min} < t < t_{\rm max}, \end{aligned} \tag{42}$$

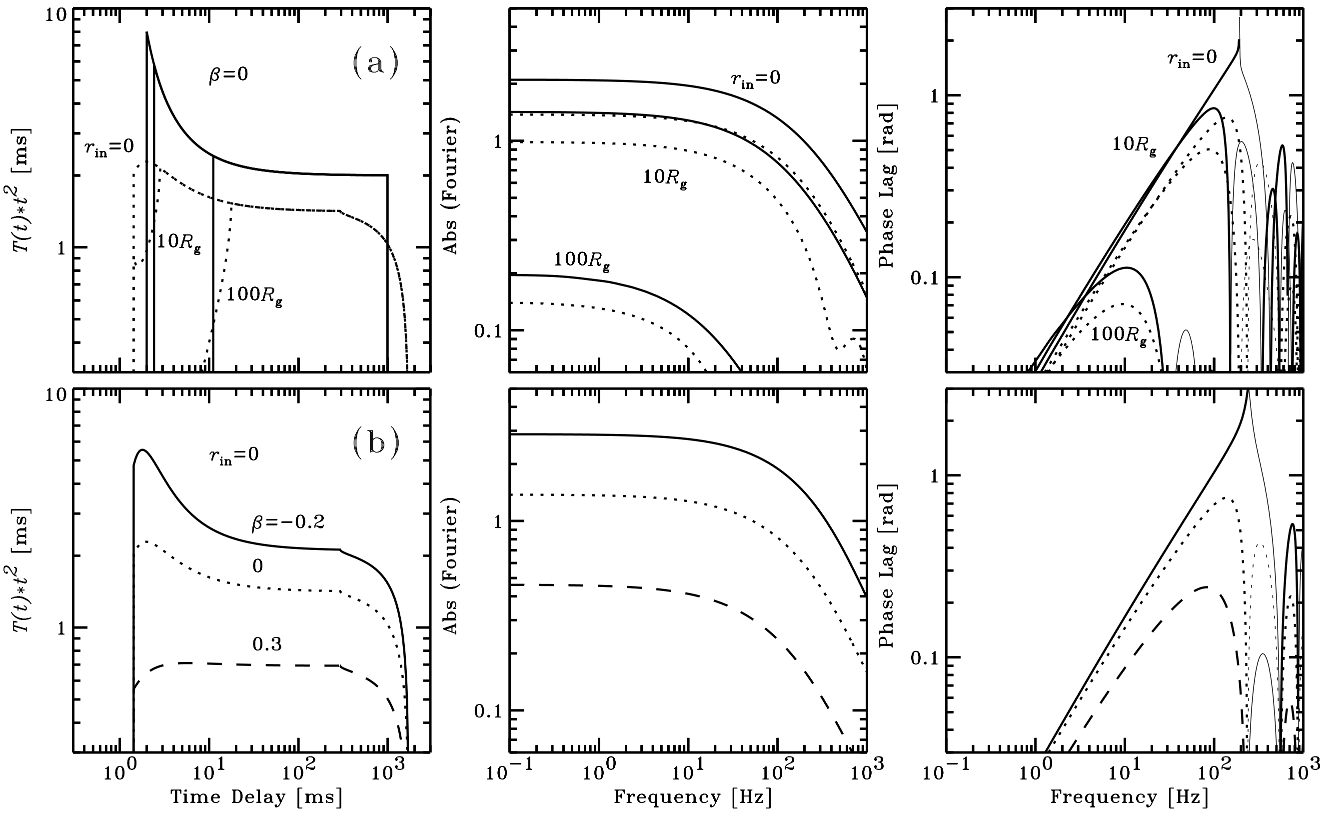

Figure 3. (a) Response functions $T(t)$ (in the isotropic approximation), their Fourier amplitudes, and the phase lags for the flat disc with different inner radius $r_{\rm in}$ and $r_{\rm out} = 10^4 R_{\rm g}$. Since asymptotically at large t in flat discs $T(t) \sim t^{-2}$, the responses are multiplied by t^2. The phase lags are computed assuming albedos $a_1 = 0, a_2 = 1$. Solid and dotted curves correspond to $\cos i = 1$ and 0.7, respectively. Thin curves give negative phase lags. (b) Dependence on the bulk velocity $\beta = v/c$. Solid, dotted, and dashed curves correspond to $\beta = -0.2, 0, 0.3$, respectively. Parameters are $r_{\rm in} = 0$, $r_{\rm out} = 10^4 R_{\rm g}$, $\cos i = 0.7$. The negative β means the bulk velocity directed towards the disc. $R_{\rm g}/c = 10^{-4}$ s in all simulations.

where

$$\begin{aligned} t_{\min} &= \max(2h\cos i, \sqrt{r_{\rm in}^2 + h^2} + h\cos i - r_{\rm in}\sin i), \\ t_{\max} &= \sqrt{r_{\rm out}^2 + h^2} + h\cos i + r_{\rm out}\sin i, \end{aligned} \tag{43}$$

and the limits

$$\begin{aligned} p_{\rm m} &= \max(\sqrt{r_{\rm in}^2 + h^2}, p_-), \\ p_{\rm M} &= \min(\sqrt{r_{\rm out}^2 + h^2}, p_+), \\ \theta_{\rm m,M} &= \arccos[(p_{\rm m,M} - q)/s]. \end{aligned} \tag{44}$$

For $\sqrt{r_{\rm in}^2 + h^2} + h\cos i + r_{\rm in}\sin i \le t \le \sqrt{r_{\rm out}^2 + h^2} + h\cos i - r_{\rm out}\sin i$, the response function is given by equation (40). Fig. 3a shows the response function and other timing characteristics for different inner radii $r_{\rm in}$. Since in flat discs $T(t) \sim t^{-2}$ at large t (see eq. [40]), the responses are multiplied by t^2. Due to the absence of the reflector in the direct vicinity of the flare, reflection acts as a low pass filter removing high frequency signal from the reflected radiation. This causes the maximum of the phase lag to shift to lower frequencies. For large $r_{\rm in}$, the covering factor of the reflector is small and therefore the amplitude of the phase lag decreases.

4.2.3 *Anisotropic sources*

Let us consider anisotropic sources of radiation. When the X-ray emitting plasma has some bulk velocity $\beta \equiv v/c$ away from or towards the disc, the angular distribution of the radiation is

$$\Omega(\mu) = \frac{1}{\gamma^4(1-\beta\mu)^3}, \quad \gamma = 1/\sqrt{1-\beta^2}, \tag{45}$$

if the emission is isotropic in the plasma rest frame (see e.g. Rybicki & Lightman 1979). This formula is valid for both the bolometric luminosity as well as for the monochromatic luminosity for a photon spectral index $\Gamma = 2$. Similarly to derivations in § 4.2.1, we then can analytically compute the infinite slab response function substituting $\Omega(-h/p)$ to equation (20) :

$$\begin{aligned} T_\beta(t) = \; & \frac{2h}{\pi}(1-\beta\cos i)^3 \int_0^\pi \frac{{\rm d}\theta}{p^2(1+\beta h/p)^3} \\ = \; & \frac{2h}{\pi}(1-\beta\cos i)^3 \sum_{k=0}^\infty \frac{(k+1)(k+2)}{2}(-\beta h)^k \\ \times \; & \int_0^\pi \frac{{\rm d}\theta}{(q+s\cos\theta)^{k+2}} \\ = \; & h(1-\beta\cos i)^3 \sum_{k=0}^\infty (k+1)(k+2)(-\beta h)^k \\ \times \; & \frac{P_{k+1}\left(q/\sqrt{q^2-s^2}\right)}{(q^2-s^2)^{1+k/2}}, \end{aligned} \tag{46}$$

where P_k are the Legendre polynomials and we used relation 3.661 from Gradshteyn & Ryzhik (1980) to obtain the last expression.

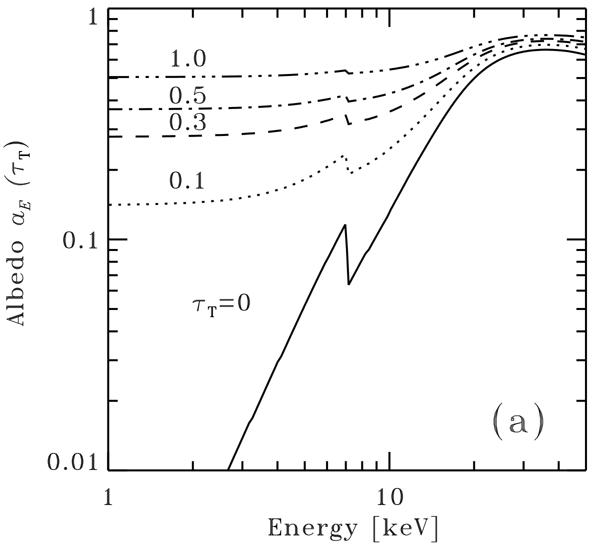

Figure 4. (a) Energy dependence of the reflection albedo for a slab with purely scattering skin of Thomson thickness $\tau_{\rm T}$ atop of a neutral slab. (b) Energy dependence of the phase lags. An isotropic X-ray source is elevated at $h = 10$ above an infinite "ionised" slab. The phase lags are computed relative to $E_1 = 3$ keV at Fourier frequency $f = 1/(10h)$ (i.e. 100 Hz for $h = 10R_{\rm g} = 3\ 10^7$ cm).

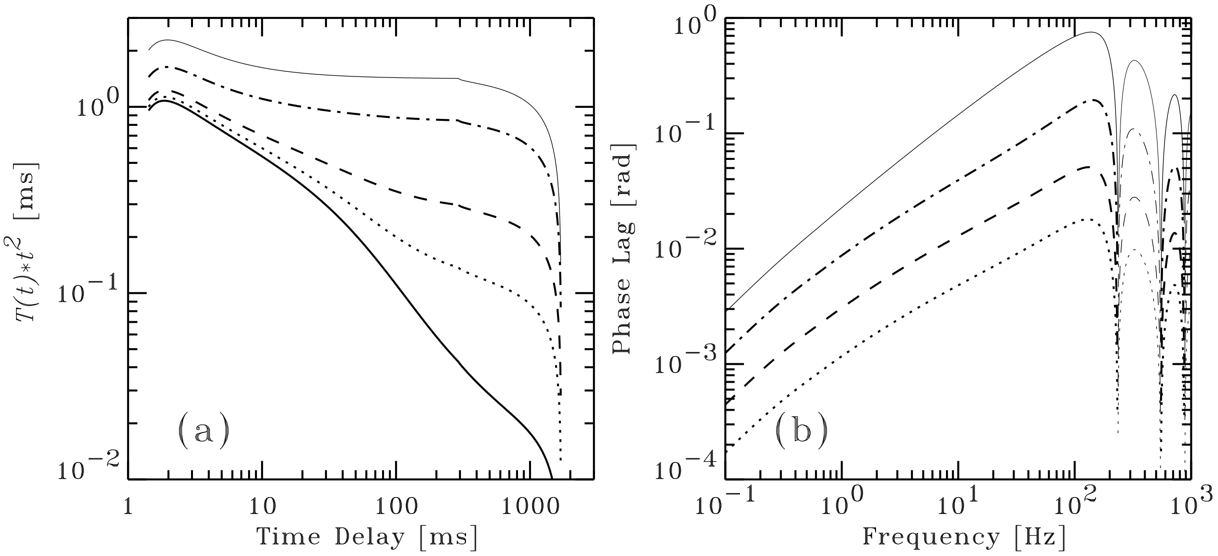

Figure 5. (a) Response functions $T_E(t)$ for a flat slab with ionised skin which optical depth decreases with radius as $\tau_T(r) = \tau_0(1 + r/10h)^{-3/2}$, where $\tau_0 = 1$, and $h = 10$ are assumed (here cos $i = 0.7$ and $R_{\rm g} = 3\ 10^6$ cm). Thick curves from the bottom to the top correspond to 3, 6, 12, 24 keV. Thin solid curve represents the response function with unity albedo over the whole surface. (b) Corresponding phase lags relative to 3 keV. Thin solid curve represents the case of constant albedos $a_2 = 1, a_1 = 0$.

The responses together with the related phase lags are presented in Fig. 3b for a few β. With increasing β, the response amplitude decreases since radiation is becoming more beamed away from the disc towards the observer. At small lags the effect is even more dramatic. This causes also a significant change in the amplitude of the phase lags at high frequencies.

4.2.4 Ionised discs

The intense incident X-ray flux can affect the ionisation state of the reflecting material changing its albedo. The surface layer of the accretion disc is heated up to the Compton temperature of radiation and is almost completely ionised (e.g. Nayakshin, Kazanas & Kallman 2000). We can consider such "skin" as a purely scattering medium. A transition layer from the hot layer to almost neutral matter is very thin. Therefore, a two-phase model, with a hot layer atop of neutral material, can be adopted. We neglect smearing of the reflection features by thermal motions in the skin and consider pure Thomson scattering.

One should point out here that in the isotropic approximation, the response functions $T(t)$ given by equation (20) are not affected by ionisation (while the reflected luminosity is affected). However, the phase lags at given energies will change since they depend on the reflection albedo. If reflection from the underlying neutral material follows Lambert's law (i.e isotropic intensity), the total reflection albedo can be expressed as follows (Sobolev 1975):

$$a(\zeta, \tau_{\rm T}) = 1 - 2(1-a)\frac{1 + \frac{3}{2}\zeta + \left(1 - \frac{3}{2}\zeta\right)\exp(-\tau_{\rm T}/\zeta)}{4 + 3\tau_{\rm T}(1-a)}, \quad (47)$$

where $\tau_{\rm T}$ is Thomson optical thickness of the ionised layer, and a is the albedo for a neutral slab. The angle averaged albedo is then

$$
\begin{aligned}
a(\tau_{\rm T}) &= 1-(1-a)\frac{7-3\exp(-\tau_{\rm T})+(4+3\tau_{\rm T})E_2(\tau_{\rm T})}{2[4+3\tau_{\rm T}(1-a)]} \\
&\approx 1-(1-a)\frac{7+\exp(-10\tau_{\rm T})}{2[4+3\tau_{\rm T}(1-a)]}, \qquad (48)
\end{aligned}
$$

where E_2 is the exponential integral of the 2nd order. A relative error of the approximation in the nominator is smaller than 1% for any $\tau_{\rm T}$. The energy dependence of the albedo for different $\tau_{\rm T}$ is shown in Fig. 4a. We see that at lower energies the albedo is high, $a_{\min}(\tau_{\rm T}) \approx 3\tau_{\rm T}/(4+3\tau_{\rm T})$, compared with the neutral material albedo, and therefore one cannot assume $a_1 \ll 1$ when computing the phase lags. The important quantity here is, however, not the albedo itself, but the difference between albedos at different energies (see eqs. 29, 30):

$$
\begin{aligned}
a_2(\tau_{\rm T})-a_1(\tau_{\rm T}) &\approx \frac{(a_2-a_1)\{1-[1-\exp(-10\tau_{\rm T})]/8\}}{[1+3\tau_{\rm T}(1-a_1)/4][1+3\tau_{\rm T}(1-a_2)/4]} \\
&\approx \frac{a_2-a_1}{(1+3\tau_{\rm T}/4)^2}. \qquad (49)
\end{aligned}
$$

The first approximate formulae is accurate within 1%. The accuracy of the second one is better than 13% for $\tau_{\rm T} < 0.5$, and is better than 20% upto albedo $a_2 \sim 0.7$ (i.e. $E \sim 20$ keV) for $\tau_{\rm T} \sim 1$. The resulting phase lags (relative to 3 keV) at $f = 1/(10h)$ as a function of photon energy are shown in Fig. 4b. They have very similar behaviour at other frequencies (see Fig. 2) and follow the $a_2(\tau_{\rm T}) - a_1(\tau_{\rm T})$ dependence (see eq. 29).

In real physical situations, the optical depth of the ionised skin could be a function of the radius. For a source of ionising radiation at the disc axis at height h, we can approximate the radial distribution as $\tau_{\rm T}(r) = \tau_0(1+r/10h)^{-3/2}$ (see e.g. Nayakshin 2000). The resulting response functions $T_E(t)$ computed from equation (12) in isotropic approximation are shown in Fig. 5a. Close to the center (small delays), the responses for different energies are close to each other, due to the fact that the effective albedo is large for all energies (see eq. [48]). At large delays, a strong energy dependence of the effective albedo results in large differences in the responses. The response is strongly suppressed at small energies, while at higher energies the shape of the response function is similar to the constant albedo case. The resulting phase lags (see Fig. 5b) are then smaller (comparing to the constant albedo case) at higher frequencies since the difference of the albedos becomes smaller (see eqs. [29, 30, 49]). Phase lags at low frequencies are hardly affected by ionisation.

4.3 Flared disc response

An important parameter influencing the response of a flared disc is the α-parameter (see eq. 1) which describes the disc shape. In the general case, it is difficult to get useful analytical formulae for the disc response, therefore we compute the responses numerically (see eq. [20] and Appendix). We first consider an isotropic source above the disc and vary the α-parameter. The results are shown in Fig. 6a. For $\alpha = 1$ the response does not differ much from that of the flat disc. For any $\alpha > 1$, there appears an increased response from the outer part of the disc and the response function flattens out at large lags. Comparing with the flat discs (and flared discs with $\alpha = 1$), the additional phase lags corresponding to the light crossing time to the outer part of the disc $\tau \sim r_{\rm out}/c$ appears at low frequencies $f \sim 1/(2\pi\tau)$. The larger the curvature (i.e. larger α), the more prominent the bump in the Fourier-frequency–dependent phase lag spectrum becomes.

Changes of the accretion disc size affect mostly the lags at low frequencies corresponding to the response from the outer edge (Fig. 6b). For larger $r_{\rm out}$, the secondary phase lag peak shifts towards lower frequencies with a constant amplitude.

Variations in the plasma bulk velocity and corresponding changes in the angular distribution of the intrinsic radiation affect markedly the flared disc response functions and the phase lags. They are presented in Fig. 6c for a few β. The most prominent effect is the dramatic change in the amplitude of the response at small lags, i.e. from vicinity of the X-ray source. The response from the outer disc edge is affected less since for $\eta \sim 0$ and mildly relativistic velocities, beaming is not so important. The resulting phase lags are affected in a similar way: the amplitude of the phase lags at high frequencies changes dramatically, while the lags at low frequencies related to the outer disc edge remain basically the same.

4.4 Approximations

4.4.1 *Accuracy of isotropic approximation*

Let us now estimate the accuracy of the isotropic approximation. Using the exact expressions for ρ_E-function (eq. 15) we computed the response functions for the two cases $\lambda = 0.1$ and 1 corresponding to the photoelectric absorption and the scattering dominated regimes. The results are shown in Fig. 7. The difference is coming from different angular dependences of the reflection Green function (15) at different λ.

For small λ, $H_\lambda \sim 1$ and $\rho_E(\cos i, \zeta)/a_E \sim 1/(\cos i + \zeta)$. At rather small inclinations, $\cos i = 0.7-1$, the reflected intensity is reduced comparing to the isotropic case ($\rho_E/a_E = 1$) at small lags (photons coming underneath the flare) since $\zeta \sim 1$. At large delays, $\zeta \sim 0$ and the reflected intensity is closer to the isotropic case. For small inclinations, $\cos i \sim 0$, the reflection is significantly larger than that given by the isotropic approximation at large delays (i.e. small ζ) (see lower panel in Fig. 7).

For $\lambda \sim 1$, $H_\lambda(\eta) \sim 1+2\eta$ and $\rho_E(\cos i, \zeta)/a_E \sim (1+2\cos i)(1+2\zeta)/4(\cos i+\zeta)$. At small inclinations, the isotropic approximation underestimates (overestimates) slightly the response at small (large) lags. At large inclinations and large delays, the response exceeds that in the isotropic approximation.

Thus, the isotropic approximation overestimates (underestimates) response at small (large) lags for most inclinations and for $\lambda \ll 1$. For $\lambda \sim 1$, the isotropic approximation is very accurate at small lags. At large lags, it overestimates (underestimates) slightly response at small (large) inclinations.

The phase lags expected for the flat disc and computed using the accurate response function as well as in the isotropic approximation are presented on the right panels in Fig. 7. For $\lambda \ll 1$, the "isotropic" phase lags are larger for small inclinations and smaller for large inclinations than the accurate ones. For $\lambda \sim 1$, the phase lags computed in the isotropic approximation are almost indistinguishable from the exact ones (compare dashed and solid curves peaking at higher frequencies).

4.4.2 *Approximate response function*

Calculations of the response function from a flared disc are not entirely trivial. However, for many applications they are not even needed. One can approximate the exact results by much simpler response functions that have almost identical temporal properties.

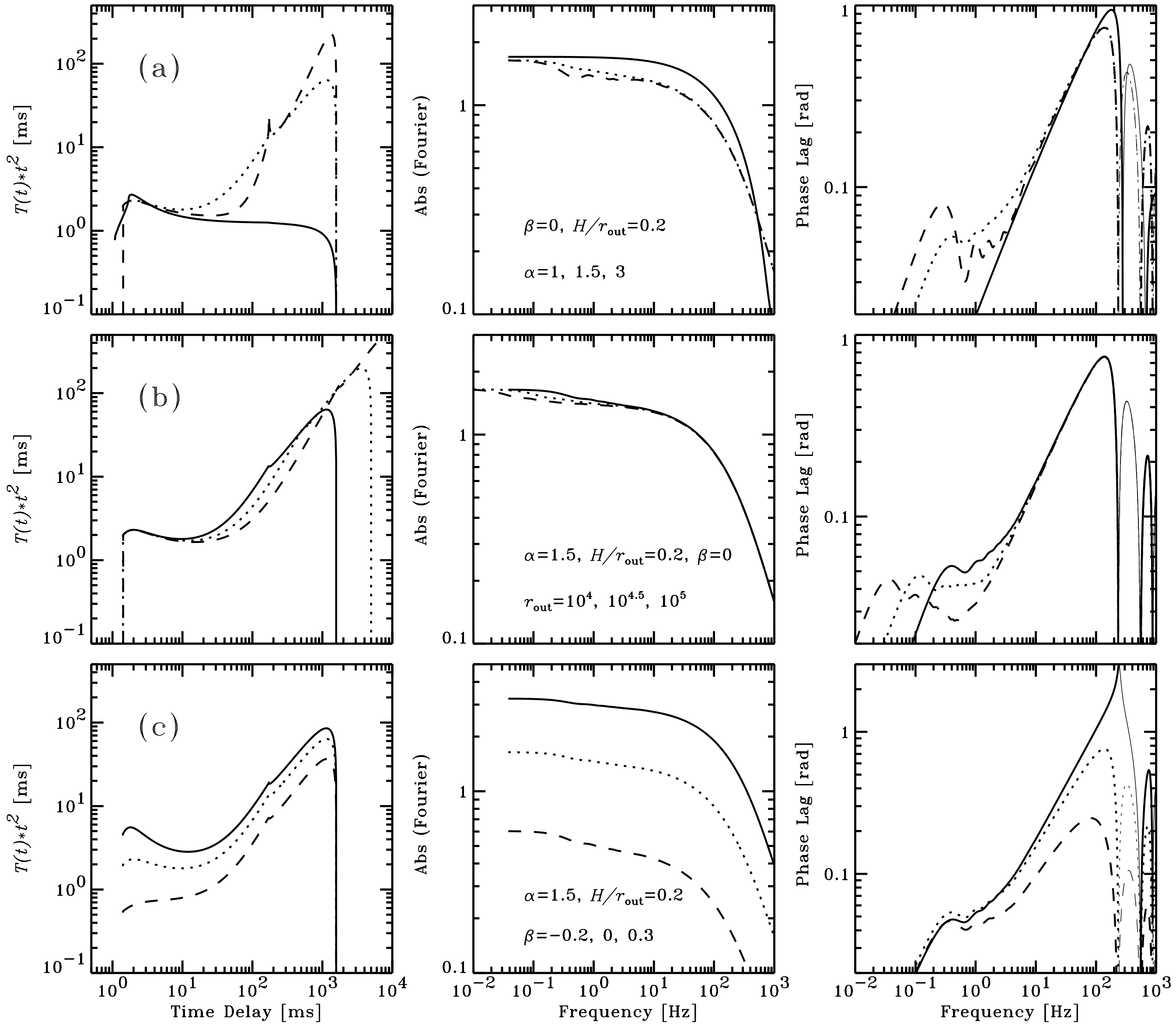

Figure 6. Response functions, their Fourier amplitudes, and the phase lags for flared discs in the isotropic approximation. The phase lags are computed assuming albedos $a_1 = 0, a_2 = 1$. Thin curves give negative phase lags. (a) Dependence on α. Solid, dotted, and dashed curves correspond to $\alpha = 1, 1.5, 3$, respectively. (b) Dependence on the outer disc radius $r_{\rm out}$. Solid, dotted, and dashed curves correspond to $r_{\rm out} = 10^4, 10^{4.5}, 10^5 R_{\rm g}$, respectively. (c) Dependence on the bulk velocity $\beta = v/c$. Solid, dotted, and dashed curves correspond to $\beta = -0.2, 0, 0.3$, respectively. Everywhere $\cos i = 0.7$, and in (a), (c) $r_{\rm out} = 10^4 R_{\rm g}$.

The reflection response from the vicinity of the X-ray source can be approximated by the flat disc response (40), while the response from the outer edge can be approximated by a power-law:

$$T_{\rm appr}(t) = R_1 T_{\rm slab}(t) + R_2 T_{\rm out}(t), \tag{50}$$

where $T_{\rm out}(t) = c\, t^{-2+1.6(\alpha-1)^{1/3}}$, $t_{\rm min} < t < r_{\rm out}$, and the constant c is found from the normalization condition $\int T_{\rm out}(t){\rm d}t = 1$. We find that the resulting phase lags are similar to the exact ones (for $r_{\rm in} \neq 0$) if one takes

$$t_{\rm min} = \begin{cases} \sqrt{r_{\rm in}^2 + h^2} + h\cos i, & x \geq 1, \\ (1-x)2h\cos i + x(\sqrt{r_{\rm in}^2 + h^2} + h\cos i), & x < 1, \end{cases} \tag{51}$$

where $x = r_{\rm in}/h\tan i$. The normalisation factors, i.e. the apparent amplitude of reflection from the disc area close to the source and that from the outer edge, depend on the inclination, bulk velocity β, and solid angle occupied by the outer disc edge expressed in $H/r_{\rm out}$:

$$R_1 = \int_{-1}^{0} {\rm d}\mu \frac{\Omega(\mu)}{\Omega(\cos i)} = (1-\beta\cos i)^3 \frac{1+\beta/2}{(1+\beta)^2}, \tag{52}$$

$$\begin{aligned} R_2 &= \frac{H}{r_{\rm out}} \int_0^{H/r_{\rm out}} {\rm d}\mu \frac{\Omega(\mu)}{\Omega(\cos i)} \\ &= \frac{H}{r_{\rm out}} (1-\beta\cos i)^3 \frac{1-(\beta/2)H/r_{\rm out}}{(1-\beta H/r_{\rm out})^2}. \end{aligned} \tag{53}$$

A more accurate approximation can be introduced if one replaces the first term in equation (50) by the "anisotropic" response (46):

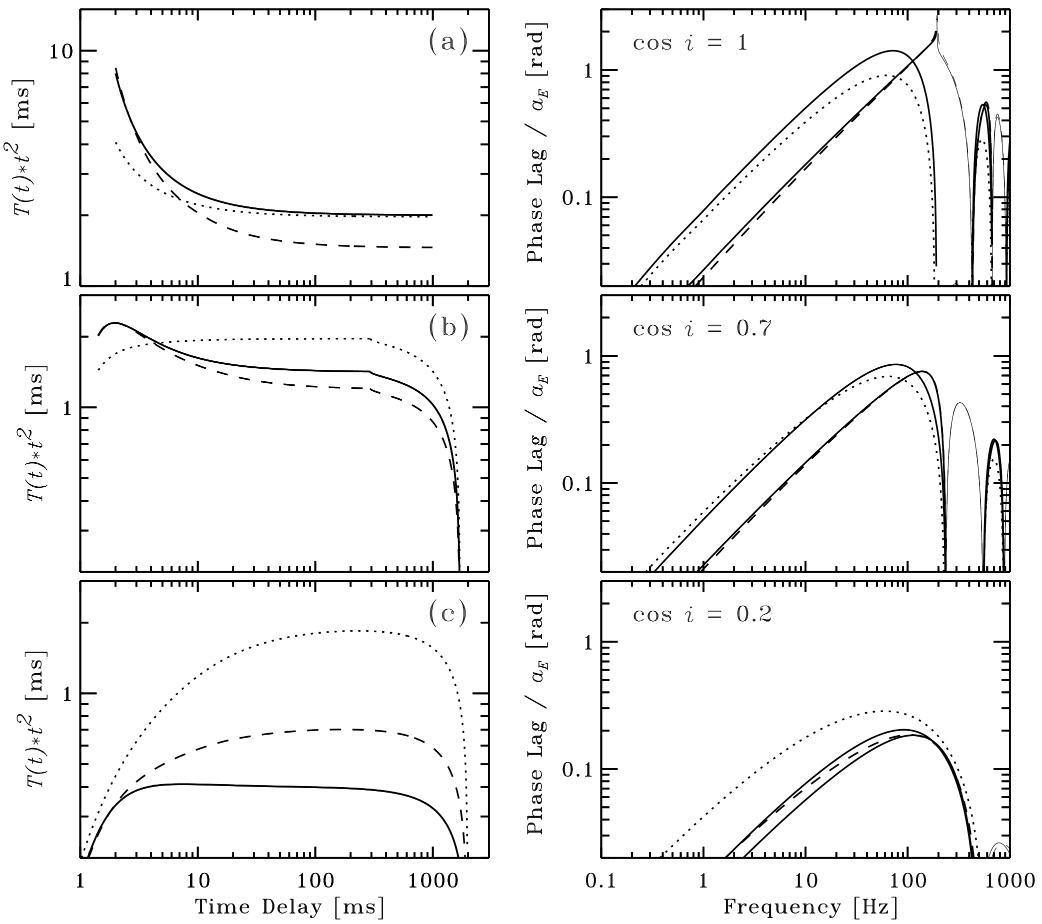

Figure 7. Response functions and phase lags for the flat disc of radius $r_{\rm out} = 10^3$ with an isotropic source at elevation $h = 10$ computed for three inclinations $\cos i = 1, 0.7, 0.2$ (from top to bottom). Dotted and dashed curves represent the response function $T_E(t)$ given by equation (12) computed using the exact angle-dependent expression for ρ_E from equation (15) for $\lambda = 0.1$ and 1, respectively, and divided by the angle-averaged albedo for these λ (i.e. by $a_E = 0.026$ and 1, see eq. [17]). The corresponding phase lags (computed assuming $a_1 = 0$) are also divided by a_E. Thin curves give negative lags. Solid curves correspond to the response function (20) computed assuming isotropic intensity of the reflected radiation, i.e. $\rho_E = a_E$. The phase lags are computed taking the same angle-averaged albedos, $a_E = 0.026$ and 1. For larger albedo, the phase lags peak shifts to higher frequency.

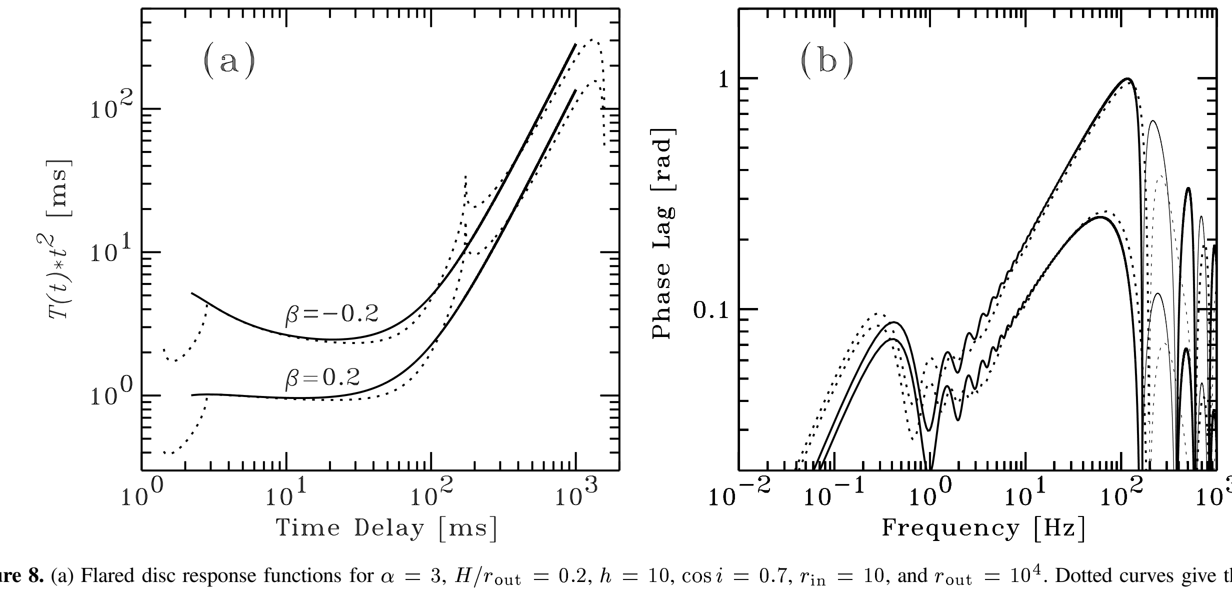

Figure 8. (a) Flared disc response functions for $\alpha = 3$, $H/r_{\rm out} = 0.2$, $h = 10$, $\cos i = 0.7$, $r_{\rm in} = 10$, and $r_{\rm out} = 10^4$. Dotted curves give the exact responses for $\beta = -0.2$ (upper curve) and $\beta = 0.2$ (lower curve). Solid curves represent the approximate response function (54). (b) Corresponding phase lags (computed for $a_1 = 0, a_2 = 1$).

$$T_{\rm appr}(t) = T_\beta(t) + R_2 T_{\rm out}(t). \quad (54)$$

This approximation is compared with the accurate response functions for flared discs at Fig. 8. One sees that it reproduces rather well the response functions. The approximation slightly overestimate (by 30% – 50%) the position of the peak in the phase lag spectra resulting in a similar error in estimation of the disc radius.

5 COMPARISON WITH OBSERVATIONS AND DISCUSSION

The phase lag Fourier spectra of a number of GBHs show breaks and secondary peaks at low frequencies (Nowak et al. 1999a,b; Grove et al. 1998; see Fig. 9). The appearance of a secondary peak could be related to the variability properties of the intrinsic signal. The peaks in the phase lag spectra approximately correspond to the peaks in the power density spectra in the $fP(f)$ representation (see e.g. Nowak et al. 1999a; Kotov, Churazov & Gilfanov 2001) which can be produced by two independent processes. The secondary phase lag peaks can also be a result of reflection from the outer part of the disc (Poutanen 2001). The position of these peaks would then depend on the disc size (see Fig. 6b). For a linear response, the energy dependence of the lags at a given frequency should have features characteristic of reflection: an Fe line, an edge, and hardening above 10 keV. The lags observed in Cyg X-1 at frequencies above 0.6 Hz do not show these features (Kotov et al. 2001). In fact, the reflection features appear to have negative contribution ("anti-lags"), i.e. the lags are *reduced* at energies where reflection is expected to contribute. This could be interpreted as a non-linear, negative response. At lower frequencies (below 0.6 Hz), the energy dependence of lags is not known. It is possible that there the reflection response is still positive and the lag energy dependence shows reflection features.

Let us develop a toy model that is capable of describing the observed phase lags (and the PDS). We assume that the lags at high frequencies are intrinsic, i.e. related to the direct radiation. We describe the direct emission in terms of a simple modified shot noise model. The shot profile is taken to be a rising exponential $\exp(t/t_E),\ t<0$. For a power law radiation spectrum with time-varying spectral index, the shot time-scale depends logarithmically on energy $t_E = t_0[1-b\ln(E/E_0)]$ (see Poutanen & Fabian 1999; Kotov et al. 2001). Spectral evolution can for example be produced by evolution of magnetic flares (Poutanen & Fabian 1999). We consider b as a free parameter since its value is determined by the details of spectral evolution which are unknown. The decreasing of t_E with energy ensures that the ACF width decreases with E as observed (Maccarone et al. 2000). The resulting CCFs peak at zero lag since the shots at different energies are correlated and peak at the same time. For a given t_0, the cross-spectrum of the signal at two energies is $\hat{C}(f,t_0) \propto t_1 t_2/[(1-i2\pi f t_1)(1+i2\pi f t_2)]$. If t_0 is distributed according to $P(t_0)$, the total cross-spectrum becomes $\hat{C}(f) = \int \hat{C}(f,t_0) P(t_0) {\rm d}t_0$. We assume a power-law distribution $P(t_0)\propto t_0^{-p}$ between $t_{\min}$ and $t_{\max}$. The lags observed from Cyg X-1 on 1996, October 22 (Nowak et al. 1999a) at high frequencies can be described by this model (dashed curves in Fig. 9) with $t_{\max}=0.05$ s, $p=1.5$, $b=0.22$, and any sufficiently small $t_{\min}$. At $f<1/(2\pi t_{\max})$, phase lags are proportional to f. With these parameters, the PDS of Cyg X-1 above 1 Hz is also well reproduces ($p=1.5$ gives the slope of the PDS also equal to 1.5, see Poutanen & Fabian 1999). The PDS shape at lower frequencies can be reproduced for example by the flare avalanches.

Let us now consider the effect of reflection by applying an approximate response function for a flared disc given by equation (54). A rather good fit to the data can be achieved for the disc inner and outer radii $30R_{\rm g}$ and $1000R_{\rm g}$, respectively, and the flaring parameter $H/r_{\rm out}=0.3$ (see Fig. 9, we assumed $\beta=0$, $\cos i=0.7$, and $\alpha=3$). One can see that reflection, however, cannot reproduce the observed sharp features. For the given parameters, the amplitude of reflection is close to that observed in Cyg X-1 (e.g. Gierliński et al. 1997; Poutanen 1998). In order not to overproduce lags at high frequencies, the reflection should be suppressed at small distances from the central source. This can be achieved by truncation of the disc at $\sim 30R_{\rm g}$(as here), by ionisation of the disc, or beaming of the radiation away from the disc. A rather small size of the disc is consistent with the fact that Cyg X-1 is probably accreting via wind from the high-mass companion. The angular momentum of accreting material is then small and the disc is small (Illarionov & Sunyaev 1975; Beloborodov & Illarionov 2001). In low-mass X-ray binaries where material accretes via Roche lobe overflow, the angular momentum is high and the disc is large. In such systems the phase lag secondary maxima should appear at lower frequencies as seems to be the case (Nowak et al. 1999b; Grove et al. 1998). Thus, if the model is correct, the disc size can be determined from the position of the phase lag peak. The lags energy dependence at low frequencies can resolve the issue whether the phase lag breaks are due to reflection.

Revnivtsev, Gilfanov & Churazov (1999) showed that the frequency-resolved spectra (proportional to the amplitude of the Fourier transforms $\hat{L}_E^{\rm D}(f)$ at a given frequency f as a function of E) of Cyg X-1 depends on frequency. At $f>20$ Hz, the spectra are rather hard and contain no reflection features. At low frequencies (below 0.1 Hz), the spectra are much softer and show strong reflection features. If the response is linear, reflection modifies the frequency resolved spectra in the following way $|\hat{L}_E(f)| \approx |\hat{L}_E^{\rm D}(f)|[1+a_E\Re\hat{T}(f)]$ (see also eqs. 26, 31). The straightforward explanation of the observed effects as solely caused by the finite light crossing time (studied in the present paper) fails, since the delays due to reflection cannot change the slope of the underlying spectra. The observed behaviour implies that the intrinsic (Comptonized) frequency-resolved spectra, $\hat{L}_E^{\rm D}(f)$, depend on frequency. In that case, the signal at different frequencies possibly is produced in physically different locations. For example, the high frequency signal can be produced closer to the black hole, while the low frequency signal–further away. This arrangement would be natural if the dominant frequencies are the Keplerian ones. However, physically different locations also imply different reflection response functions thus complicating the situation.

The X-ray reprocessing in the cool disc produces both the Compton reflection continuum with an Fe line and soft radiation. The reprocessed radiation from the outer disc emerges in the optical/UV bands. The response function of this soft radiation to the variability of the intrinsic X-ray radiation would be similar to that of the Compton reflection continuum unless ionisation state of the reflecting material is a function of radius. Thus, the accretion disc response function obtained from the cross-correlation analysis of the optical and the X-ray light curves (see e.g. Hynes et al. 1998; O'Brien & Horne 2001) should also satisfy the constraints coming from the X-ray timing e.g. from the Fourier-frequency–dependent phase lags. If the response is known from the optical/X-ray data, then one can try to subtract the lags related to the reflection from the observed time lags in order to obtain the lags corresponding to the intrinsic (direct) signal only. This will not be easy, however, if

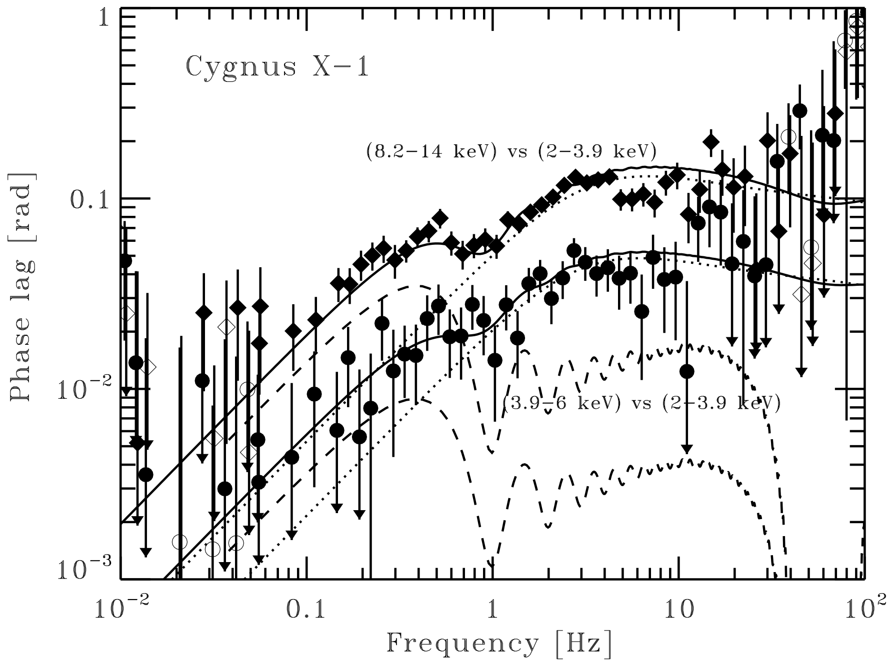

Figure 9. Phase lags between signals in the 8.2-14 keV and the 3.9-6 keV bands vs the 2-3.9 keV band observed with *RXTE* in Cyg X-1 on 1996, October 22 (Nowak et al. 1999a; Pottschmidt et al. 2000). Dotted curves correspond to the intrinsic lags described by a modified shot noise model (Poutanen & Fabian 1999) with exponentially rising shots of time-scale t_0 distributed between 1 ms and 0.05 s according to a power law $P(t_0) \propto t_0^{-p}$ with $p = 1.5$. At a given energy E the shot time-scale is $t_E = t_0[1 - b\ln(E/E_0)]$, where $E_0 = 3$ keV and $b = 0.22$. Since t_E decreases with energy, the lags are hard. Dashed curves are the lags produced by reflection from a flared disc with the following parameters $r_{\rm in} = 10$, $r_{\rm out} = 10^3$, $h = 10$ (in units $R_{\rm g} = 3\ 10^6$ cm), $H/r_{\rm out} = 0.3$, $\alpha = 3$, $\cos i = 0.7$, and $\beta = 0$. Solid curves give the sum of the lags from the intrinsic signal and reflection.

the reflection response is non-linear or the disc is ionised (then the UV and Compton reflection responses are different).

Real accretion discs are not necessarily axisymmetric, but can be, for example, radiatively warped (e.g. Pringle 1996; Wijers & Pringle 1999) or warped due to the Bardeen–Peterson (1975) effect. For non-axisymmetric discs the response function depends not only on the inclination, but also on the azimuthal angle. Blackman (1999) and Hartnoll & Blackman (2000) studied the Fe line profiles produced in flared axisymmetric and warped discs. It would be interesting to study temporal response of the iron line profile for such discs. If reflection is responsible for shaping the phase lags, they would change periodically depending on the azimuthal angle.

We focused on the effects of Compton reflection on temporal characteristics and not much attention was paid to the iron emission line. With future instruments of high spectral resolution and large effective area, it will be possible to study the phase lags across the line profile. By combining the line profile with the energy dependence of the phase lags it will be possible to put better constraints on the accretion disc geometry in X-ray binaries. The narrow cores, produced in the material far away from the X-ray source, would be associated with large time delays. The broad wings should respond faster to the variations of the continuum and the lags should be smaller. However, there could be serious complications. We assumed everywhere that there is a linear response between variations of the continuum and the reflected radiation. In other words, properties of the reflecting material are assumed to be constant independently of the X-ray flux. This assumption could be wrong since the ionisation state of the reflecting material depends on the illuminating flux (see e.g. Reynolds 2000; Nayakshin & Kazanas 2001).

Another complication is that the angular distribution of the intrinsic radiation could change. This would be likely for example in the model with mildly-relativistic outflows (Beloborodov 1999; Malzac, Beloborodov & Poutanen 2001). If the velocity of the plasma ejection is correlated with the energy dissipation rate in magnetic flares, one could expect that a large emitted luminosity corresponds to a larger ejection velocity, and more beaming away from the disc. This would decrease the amplitude of reflection at large fluxes. The resulting reflection response could thus be non-linear possibly reproducing negative lags introduced by reflection (Kotov et al. 2001). Further studies in that direction are in progress.

6 CONCLUSIONS

In the present paper, we have developed the formalism for computing the response functions for isotropic and anisotropic X-ray sources above flat and flared accretion discs. We have also studied the impact of the reflection on the temporal characteristics such as the power density spectra, auto- and cross-correlation functions, and the Fourier-frequency–dependent time/phase lags. A number of useful approximations was introduced to simplify significantly computations of the response function. Simple approximate response function was shown to have temporal characteristics which are very similar to that computed using exact responses.

The temporal characteristics predicted by a model with a linear response of the reflected component onto the variability of the intrinsic radiation were computed. The reflection model can reproduce the observed secondary maxima at low frequencies in the phase lag Fourier spectra of Cyg X-1 and other GBHs. The position of these maxima could be used to get constraints on the accretion disc size. In spite of the fact that the observed energy dependence of the phase lags at high frequencies indicate that reflection is not their only source (Kotov et al. 2001), a proper account of the impact of the reflection on temporal characteristics is necessary, when interpreting the data.

ACKNOWLEDGMENTS

This work was supported by the Swedish Natural Science Research Council and the Anna-Greta and Holger Crafoord Fund. The author is grateful to Andrei Beloborodov and an anonymous referee for useful comments that significantly improved the paper.

REFERENCES

Bardeen J. M., Petterson J. A., 1975, ApJ, 195, L65
Basko M. M., Sunyaev R. A., Titarchuk L. G., 1974, A&A, 31, 249
Beloborodov A. M., 1999, ApJ, 510, L123
Beloborodov A. M., Illarionov A. F., 2001, MNRAS, 323, 167
Blackman E. G., 1999, MNRAS, 306, L25
Chandrasekhar S., 1960, Radiative Transfer. Dover, New York
Done C., Życki P. T., 1999, MNRAS, 305, 457
Esin A. A., Narayan R., Cui W., Grove J. E., Zhang S.-N., 1998, ApJ, 505, 854
Fabian A. C., Iwasawa K., Reynolds C. S., Young A. J., 2000, PASP, 112, 1145
George I. M., Fabian A. C., 1991, MNRAS, 249, 352
Ghisellini G., Haardt F., Matt G., 1994, MNRAS, 267, 743
Gierliński M., Zdziarski A. A., Done C., Johnson W. N., Ebisawa K., Ueda Y., Haardt F., Phlips B. F., 1997, MNRAS, 288, 958
Gilfanov M., Churazov E., Revnivtsev M., 1999, A&A, 352, 182
Gilfanov M., Churazov E., Revnivtsev M., 2000a, in Zhao G., Wang J. J., Qiu H. M., Boerner G., eds, SGSC Conference Series Vol. 1, 5th Sino-German Workshop on Astrophysics. China Science & Technology Press, Beijing (astro-ph/0002415)
Gilfanov M., Churazov E., Revnivtsev M., 2000b, MNRAS, 316, 923
Gradshteyn I. S., Ryzhik I. M., 1980, Table of Integrals, Series, and Products. Academic Press, New York
Grove J. E., Strickman M. S., Mats S. M., Hua X.-M., Kazanas D., Titarchuk L. G., 1998, ApJ, 502, L45
Guainazzi M., et al. 1998, MNRAS, 301, L1
Hartnoll S. A., Blackman E. G., 2000, MNRAS, 317, 880
Hynes R. I., O'Brien K., Horne K., Chen W., Haswell C. A. 1998, MNRAS, 299, L37
Illarionov A. F., Sunyaev R. A., 1975, A&A, 39, 185
Kotov O., Churazov E., Gilfanov M., 2001, MNRAS, 327, 799
Lee J. C., Fabian A. C., Reynolds C. S., Brandt W. N., Iwasawa K., 2000, MNRAS, 318, 857
Maccarone T. J., Coppi P. S., Poutanen J., 2000, ApJ, 537, L107
Magdziarz P., Zdziarski A. A., 1995, MNRAS, 273, 837
Malzac J., Beloborodov A. M., Poutanen J., 2001, MNRAS, 326, 417
Mason K. O., Cordova F. A., 1982, ApJ, 262, 253
Miyamoto S., Kimura K., Kitamoto S., Dotani T., Ebisawa K., 1991, ApJ, 383, 784
Nandra K., Pounds K. A., 1994, MNRAS, 268, 405
Nayakshin S., 2000, ApJ, 534, 718
Nayakshin S., Kazanas D., Kallman T. R., 2000, ApJ, 537, 833
Nayakshin S., Kazanas D., 2001, ApJ, submitted (astro-ph/0106450)
Nolan P. L. et al., 1981, ApJ, 246, 494
Nowak M. A., Vaughan B. A., Wilms J., Dove J. B., Begelman M. C., 1999a, ApJ, 510, 874
Nowak M. A., Wilms J., Dove J. B., 1999b, ApJ, 517, 355
O'Brien K., Horne K., 2001, in Boffin H., Steeghs D., Cuypers J., eds, Astro-tomography Workshop. Springer-Verlag, Berlin, in press (astro-ph/0104428)
Papadakis I. E., Lawrence A., 1995, MNRAS, 272, 161
Pottschmidt K., Wilms J., Nowak M. A., Heindl W. A., Smith D. M., Staubert R., 2000, A&A, 357, L17
Poutanen J., 1998, in Abramowicz M. A., Björnsson G., Pringle J. E., eds, Theory of Black Hole Accretion Discs. Cambridge Univ. Press, Cambridge, p. 100
Poutanen J., 2001, AdSpR, in press (astro-ph/0102325)
Poutanen J., Fabian A. C., 1999, MNRAS, 306, L31
Poutanen J., Nagendra K. N., Svensson R., 1996, MNRAS, 283, 892
Pringle J. E., 1996, MNRAS, 281, 357
Revnivtsev M., Gilfanov M., Churazov E., 1999, A&A, 347, L23
Reynolds C. S., 1999, in Poutanen J., Svensson R., eds, ASP Conf. Series Vol. 161, High Energy Processes in Accreting Black Holes. Astron. Soc. Pac., San Francisco, p. 178
Reynolds C. S., 2000, ApJ, 533, 811
Reynolds C. S., Young A. J., Begelman M. C., Fabian A. C., 1999, ApJ, 514, 164
Rybicki G. B., Lightman A. P., 1979, Radiative Processes in Astrophysics. Wiley, New York
Shakura N. I., Sunyaev R. A., 1973, A&A, 24, 337
Smith I. A., Liang E. P., 1999, ApJ, 519, 771
Sobolev V. V., 1975, Light Scattering in Planetary Atmospheres. Pergamon Press, Oxford
Trümper J., Sztajno M., Pietsch W., van Paradijs J., Lewin W. H. G., 1985, Sp. Sci. Rev., 40, 255
Verbunt F., 1999, in Sellwood J. A., Goodman J., eds, ASP Conf. Series Vol. 160, Astrophysical Discs: An EC Summer School. Astron. Soc. Pac., San Francisco, p. 21
Vikhlinin A., 1999, ApJ, 521, L45
Vrtilek S. D., Raymond J. C., Garcia M. R., Verbunt F., Hasinger G., Kurster M., 1990, A&A, 235, 162
White N. E., Holt S. S., 1982, ApJ, 257, 318
Wijers R. A. M. J., Pringle J. E., 1999, MNRAS, 308, 207
Zdziarski A. A., 1999, in Poutanen J., Svensson R., eds, ASP Conf. Series Vol. 161, High Energy Processes in Accreting Black Holes. Astron. Soc. Pac., San Francisco, p. 16
Zdziarski A. A., Lubiński P., Smith D. A., 1999, MNRAS, 303, L11

APPENDIX A: CALCULATION OF THE RESPONSE FUNCTION

A1 Visibility conditions

Contrary to the case of the flat disc, the every point of a flared disc is not necessarily visible. For a concave disc surface, $z'' > 0$, the condition for visibility reads

$$\tan i < \frac{\sqrt{r_{\rm out}^2 - r^2 \sin^2\phi} - r\cos\phi}{H - z}. \tag{A1}$$

For a given inclination i and radius r, this translates to

$$\cos\phi < \cos\phi_0 \equiv \frac{(r_{\rm out}^2 - r^2) - (H-z)^2 \tan^2 i}{2(H-z) r \tan i}. \tag{A2}$$

According to the value of $\tan i$, the visibility condition is: (i) if $\tan i < 1/z'_{\rm max}$, then the whole disc surface is visible; (ii) if $1/z'_{\rm max} < \tan i < r_{\rm out}/H$, then the whole area $r < r_c$ is visible. For $r_c < r < r_{\rm out}$, the condition $\cos\phi < \cos\phi_0$ should be fulfilled. Here r_c is the solution of the equation $\tan i = (r_{\rm out} - r)/(H-z)$; (iii) if $\tan i > r_{\rm out}/H$, then the area $r < r_c$ is invisible. For $r > r_c$, the inequality $\cos\phi < \cos\phi_0$ gives the visible area. Here r_c is the solution of the equation $\tan i = (r_{\rm out} + r)/(H-z)$.

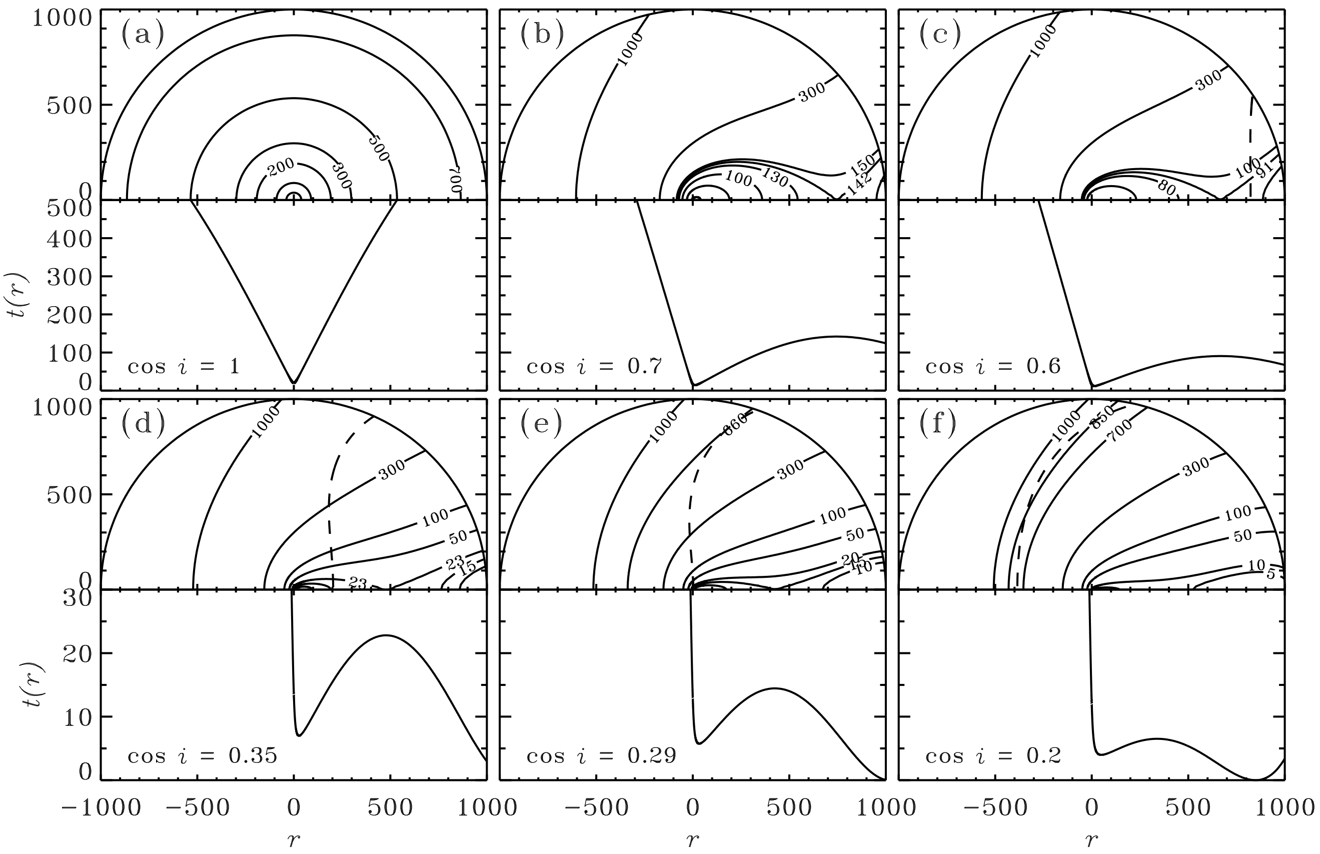

Figure 10. *Upper panels*: The curves of equal delays (isochrons) at the disc surface for different inclinations (only one half of the disc is shown). The reflector's surface is given by equation (1) with $H/r_{\rm out} = 0.3, \alpha = 3, r_{\rm out} = 1000, r_{\rm in} = 0$. The flare elevation above the disc center $h = 10$. The observer is situated in the x-z plane at inclination i. For large inclinations and certain time delays, the isochrons consist of two disconnected regions: one is close to the flare, the other one is close to the disc edge (see e.g. panels b and c). At very large inclinations, a certain area on the disc surface becomes invisible (rightwards from the dashed curves given by eq. A2). *Lower panels*: Function $t(r) = p - (z-h)\cos i - r \sin i$.

A2 Isochrons

An a given moment of time, the observer receives the signal reflected from the curve which is the interception of the paraboloid of equal delays with the disc surface. For an infinite flat disc, this curve is an ellipse with a center shifted along the x-axis:

$$\frac{(x - q\sin^2 i\ \cos i)^2}{(s/\sin i)^2} + \frac{y^2}{(s\,{\rm ctan}\, i)^2} = 1, \qquad \text{(A3)}$$

where q and s are given by equation (39). A few examples of isochrons for a flared disc are presented in Fig. 10. At small inclinations and small delays they are close to those for the flat disc (see Fig. 10b,c). The curve of equal delays on the disc surface can consist of two disconnected regions depending on the inclination, disc parameters and time. Some part of the disc can also be blocked from the observer by the disc outer edge. The area on the right side from the dashed curves on Fig. 10 is invisible.

A3 Integration over radius

Computation of the response function for flared discs is reduced to one integral over the radius (see eqs. 12, 20). For zero inclination $i = 0$, the integration is trivial using the δ-function from equation (21). For the non-zero inclination, the integration limits $r_{\rm m}$, $r_{\rm M}$ are given either by the solution of the equations

$$t = p - (z-h)\cos i \pm r\sin i, \qquad \text{(A4)}$$

or by the minimum/maximum disc radii $r_{\rm in}$, $r_{\rm out}$. Integrating over radius we use a substitution $r = [r_{\rm M} + r_{\rm m} + (r_{\rm M} - r_{\rm m})\cos\theta]/2$ which removes possible divergency of the integrand at the integration limits. The solution of equation (A4) is trivial in the case of $z = 0$ (see eqs. 39, 40). In order to solve equation (A4) for $z \neq 0$, we first tabulate the function $t(r) = p - (z-h)\cos i - r\sin i$ at a dense grid of r, with r varying between $-r_{\rm out}$ and $r_{\rm out}$. If $\tan i < r_{\rm out}/H$, equation (A4) can have from 1 up to 3 solutions (for $-r_{\rm out} < r < r_{\rm out}$). If $t'(r_{\rm out}) > 0$, then there are two solutions for $t_{\rm min} < t \le t(r_{\rm out})$ that are found by interpolation ($t_{\rm min}$ is the minimum value of $t(r)$). For $t(-r_{\rm out}) < t < t(r_{\rm out})$, $r_{\rm M} = r_{\rm out}$ and the only solution is found by interpolation ($r_{\rm m}$ is then the absolute value of that). The response function for $t \ge t(-r_{\rm out})$ is zero. If $t(r_{\rm out}) < 0$ (see Fig. 10b,c), the integral over radius has to be divided into two parts, since the isochrons consist of two separated regions for some t.

For every t, we check that the visibility condition (A2) is satisfied at all integration points θ. If the condition is not satisfied for some points, we find the radius (or radii) satisfying equation $\cos\phi(r) = \cos\phi_0(r)$ by iterations (see eqs. 22, A2). The integral is then recomputed only over radii where (A2) valid. All the routines used in this paper are written on IDL.